Research article

Comparative study of Casson hybrid nanofluid models with induced magnetic radiative flow over a vertical permeable exponentially stretching sheet

Taqi A. M. Shatnawi[1], Nadeem Abbas[2,*] and Wasfi Shatanawi[2,3,*]

[1] Department of Mathematics, Faculty of Science, The Hashemite University, P.O Box 330127, Zarqa 13133, Jordan
[2] Department of Mathematics and Sciences, College of Humanities and Sciences, Prince Sultan University, Riyadh 11586, Saudi Arabia
[3] Department of Medical Research, China Medical University Hospital, China Medical University, Taichung 40402, Taiwan

* Correspondence: Email: nabbas@psu.edu.sa, wshatanawi@psu.edu.sa.

Abstract: In this paper, the steady flow of an incompressible hybrid Casson nanofluid over a vertical permeable exponential stretching sheet is considered. The influence of the induced magnetic field is investigated. The influence of heat production and nonlinear radiation on slip effects is studied. Typically, three hybrid nanofluidic models are presented in this paper, namely: Xue, Yamada-Ota, and Tiwari Das. A study of a single-walled carbon nanotube and a multi-walled carbon nanotube with base fluid water is also provided. The governing equations are developed under flow assumptions in the form of partial differential equations by using boundary layer approximations. Using the appropriate transformations, partial differential equations are converted into ordinary differential equations. The ordinary differential equations are solved by the fifth-order Runge-Kutta-Fehlberg approach. Impacts concerning physical parameters are revealed by graphs and numerical values through tables. Temperature profile increases as concentration of solid nanoparticles increases. Because the thermal conductivity of the fluid is enhanced due to an increment in solid nanoparticles, which enhanced the temperature of the magneto-Casson hybrid nanofluid. The skin friction achieved higher values in the Yamada-Ota model of hybrid nanofluid as compared to the Xue model and Tiwari Das model. The results of this study show the Yamada-Ota model achieved a higher heat transfer rate than the Xue and Tiwari Das models of hybrid nanofluid.

1. Introduction

Energy crises are among the most pressing issues the world faces today. Several researchers discussed various methods for producing energy at a lower cost. In the past years, common fluids such as water, engine oil, and ethylene glycol had poorer heat transfer rates due to their lower thermal conductivity. Due to the higher abilities of metals, which contain more thermal conductivity properties than ordinary fluids. The nanosize metals are added to the ordinary fluids which enhance the transfer rate due to an enhancement in thermal conductivity. In real-world applications, nanofluid is used in different procedures namely nano-technological and industrial developments such as nuclear reactors, vehicle cooling, heat exchanger, etc. Furthermore, magneto nanofluids are effective in wound treatments, cancer therapy, artery blockage removal, magnetic resonance imaging, and a variety of other applications. Hamad and Bashir [1] presented the influence of nanofluid under the power law model on a vertical stretching surface. They investigated Brownian motion and thermophoresis impacts on the vertical surface in their analysis. The influence of nanofluid flow on moving surfaces was studied by Bachok et al. [2]. They also developed the results by emphasizing the effects of the plate moving in the same or opposite direction in the free stream. The study of flow of nanofluid on an exponentially stretching sheet for nanomaterial fluid flow was presented by Nadeem and Lee [3]. Bég et al. [4] studied the steady flow of magnetic hydrodynamics mixed convection of nanofluid at the permeable nonlinear stretching sheet. Ramesh [5] highlighted the effects of nanofluid with Darcy-Forchheimer over stretching sheets. Khan et al. [6] discussed the Maxwell nanofluid model on a nonlinear stretching sheet. Khan and Nadeem. [7] analyzed the influence of chemically reactive nanomaterial Casson fluid with thermal slip over an exponentially stretching surface. Ramesh et al. [8] discussed the squeezing flow of micropolar Casson nanomaterial fluid with slip effects at stretching surfaces. Recently, a few authors developed results on the boundary layer flow of nanofluid at a stretching sheet (see [9,10]).

Many interesting works have been carried out on the hybrid nanofluid, which is an extended version of nanofluid. A hybrid nanofluid is a combination of two different nanosized particles and water as the base fluid. Devi and Devi [11] emphasized the impact of hybrid nanofluid on porous sheets numerically. Heat and mass transfer of hybrid nanofluid in a circular cylinder are discussed by Nadeem et al. [12]. They considered the magnetic hydrodynamic effects under the stagnation region. Nadeem et al. [13] worked on the fluid flow of hybrid nanomaterial at curved surfaces. Abbas et al. [14] inspected the impact of hybrid nanomaterial fluid flow with inclined magnetic hydrodynamics at a nonlinear stretching cylinder. Jyothi et al. [15] discussed the Casson hybrid nanomaterial fluid with squeezing flow with a sink or source. Several authors worked on the hybrid nanofluid for different flow assumptions and various physical aspects see [16,17].

The interest in magnetic hydrodynamics with hybrid nanofluid has been developed by the authors due to its many engineering applications. Because they can be used to control the rate of heat transfer by using an external magnetic field. Ali et al. [18] studied the influence of the laminar flow of the induced magnetic field on a stretching sheet. They implemented a numerical scheme to solve nonlinear

differential equations. Thammanna et al. [19] utilized MHD to study the time-dependent flow of Casson nanomaterial fluid at an unsteadiness stretching sheet. Junoh et al. [20] emphasized the effects of the induced magnetic field with the stagnation point region. Moreover, the heat transfer rate at the stretching/shrinking sheet was analyzed by utilizing a two-phase model. Al-Hanaya et al. [21] discussed the micropolar hybrid nanomaterial fluid in the presence of a stagnation point region. They also highlighted the effects of the induced magnetic field on the curved surface. The hybrid nanomaterial fluid flow of the induced magnetic field transport mechanism has been studied by Alharbi [22]. Hafeez et al. [23] discussed the induced magnetic field of hybrid nanomaterial liquid for different aspects. Ali et al. [24] deliberated the influences of melting and MHD flow of nanomaterial liquid on the stretching surface. Some researchers have developed an interest in investigating the induced magnetic field for various flow assumptions, see [25–28].

In this study, we discuss the two-dimensional flow of Casson hybrid nanofluid over a vertical permeable exponential stretching sheet. We consider the induced magnetic field under the stagnation region. Furthermore, we discuss the effects of nonlinear radiation and heat generation. Besides, we present a study of three hybrid nanofluid models, namely: Xue, Yamada-Ota, and Tiwari Das. We also present a study on a single-wall carbon nanotube and multiwall carbon nanotube with base fluid water. We utilize boundary layer approximations to develop the governing equations under the assumptions of flow in the form of partial differential equations. Also, we use the Lie symmetry method to develop a suitable transformation. With the help of appropriate transformations, we convert partial differential equations into ordinary differential equations. Next, we use the fifth-order Runge-Kutta Fehlberg approach to analyze the ordinary differential equations. We investigate the effect of the concerning physical parameters by graphs and numerical values through tables. These findings are unique and may be helpful in the engineering and industrial fields.

2. Materials and methods

The steady flow of incompressible Casson hybrid nanofluid over a permeable exponential stretching sheet is deliberated (see Figure 1).
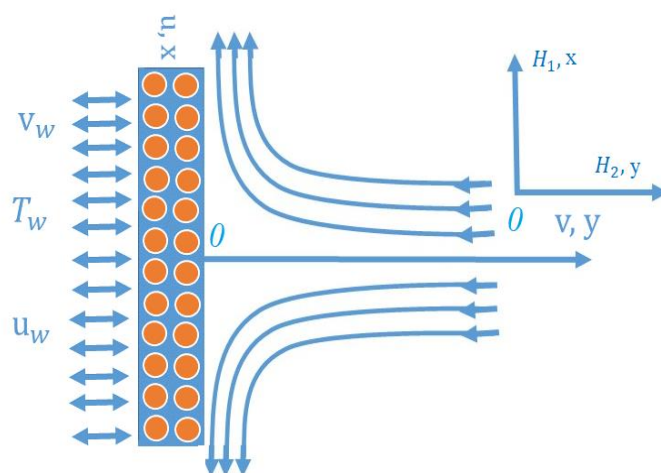
Figure 1. The flow pattern of Casson hybrid nanofluid.

The induced magnetic field is taken into account under the stagnation point flow. Heat generation and nonlinear radiation effects are discussed. The fluid wall temperature is T_w and the ambient fluid temperature is T_∞. U_e is free stream velocity, and H_e is the free stream magnetic velocity function. A mathematical model in differential form is built for flow analysis, such as (see [29–32]):

$$\frac{\partial u}{\partial x} + \frac{\partial v}{\partial y} = 0, \tag{1}$$

$$\frac{\partial H_1}{\partial x} + \frac{\partial H_2}{\partial y} = 0, \tag{2}$$

$$u\frac{\partial u}{\partial x} + v\frac{\partial v}{\partial y} - \frac{\mu_f}{4\pi p}\left(H_1\frac{\partial H_1}{\partial x} + H_2\frac{\partial H_1}{\partial y}\right) = U_e\frac{dU_e}{dx} - \frac{\mu}{4\pi p}H_e\frac{dH_e}{dx} + v_f\frac{\rho_f}{\rho_{hnf}}\left(\frac{1}{(1-\phi_1)^{2.5}(1-\phi_2)^{2.5}} + \frac{1}{\beta_1}\right)\frac{\partial^2 u}{\partial y^2} - \frac{\rho_f \mathrm{k}}{\rho_{hnf}}u, \tag{3}$$

$$u\frac{\partial H_1}{\partial x} + v\frac{\partial H_1}{\partial y} - H_1\frac{\partial u}{\partial x} - H_2\frac{\partial u}{\partial y} = \mu_e\frac{\partial^2 H_1}{\partial y^2}, \tag{4}$$

$$u\frac{\partial T}{\partial x} + v\frac{\partial T}{\partial y} = \alpha_{hnf}\frac{\partial^2 T}{\partial y^2} + Q\frac{(\rho C_p)_f}{(\rho C_p)_{hnf}}(T - T_\infty) - \frac{(\rho C_p)_f}{(\rho C_p)_{hnf}}\frac{\partial q_r}{\partial y}. \tag{5}$$

With relevant boundary conditions are as follows:

$$u = \beta^*\mu_f\left(\frac{1}{(1-\phi_1)^{2.5}(1-\phi_2)^{2.5}} + \frac{1}{\beta_1}\right)\frac{\partial u}{\partial y}, \ v = V_w, \ H_1 = 0, \ H_2 = 0, \ T = T_w + \gamma^*\frac{\partial T}{\partial y}, \text{ at } y \to 0,$$

$$u \to U_e, \ H_1 \to H_e, \ T \to T_\infty, \text{ as } y \to \infty. \tag{6}$$

Introducing the stream functions are (see [29–32])

$$u = \frac{\partial\psi}{\partial y}, \ v = -\frac{\partial\psi}{\partial x}, \ H_1 = \frac{\partial\psi_1}{\partial y}, \ H_2 = -\frac{\partial\psi_1}{\partial x}, \ T = T_\infty + (T_w - T_\infty)\theta(\eta). \tag{7}$$

$\psi_1 = H_o e^{x/2L}\sqrt{\frac{v}{U_o}}g(\eta)$ and $\psi = \sqrt{2u_o vL}e^{\frac{x}{2L}}f(\eta)$ are the stream functions of the magnetic field and velocity. By using these values, the suitable transformations can be written as

$$u = \frac{\partial\psi}{\partial y} = u_o e^{x/L}f'(\eta), \ v = -\frac{\partial\psi}{\partial x} = -\sqrt{\frac{u_o v}{2L}}e^{x/2L}(f + \eta f'), \ H_1 = \frac{\partial\psi_1}{\partial y} = \frac{H_o e^{x/2L}}{\sqrt{2L}}g'(\eta),$$

$$H_2 = -\frac{\partial\psi_1}{\partial x} = -\frac{H_o e^{x/2L}}{2L}\sqrt{\frac{v}{U_o}}(g + \eta g'). \tag{8}$$

Using the above suitable transformation, the partial differential equations are converted into ordinary differential equations as below:

$$\frac{\rho_f}{\rho_{hnf}}\left(\frac{1}{(1-\phi_1)^{2.5}(1-\phi_2)^{2.5}} + \frac{1}{\beta_1}\right)f'''(\eta) + f''f + 2(1 - f') + \gamma_1[2(g'^2(\eta) - 1) - gg''] - M\frac{\rho_f}{\rho_{hnf}}(f'(\eta) - 1) + \delta\theta = 0, \tag{9}$$

$$\lambda g'''(\eta) - gf'' + g''f = 0, \tag{10}$$

$$\frac{K_{hnf}}{K_f}\frac{(\rho_{cp})_f}{(\rho_{cp})_{hnf}}\frac{1}{Pr}\left(1 + \frac{4}{3}Rd\right)\theta'' + f\theta' + \frac{(\rho_{cp})_f}{(\rho_{cp})_{hnf}}K\theta = 0, \tag{11}$$

with boundary conditions

$$f(0) = S, \ f'(0) = \lambda_1\left(\frac{1}{(1-\phi_1)^{2.5}(1-\phi_2)^{2.5}} + \frac{1}{\beta_1}\right)f''(0), \ f'(\infty) = 1, \ g(0) = 0, \ g'(0) = 0, \ g'(\infty) =$$

$$1, \ \theta(0) = 1 + \delta_1\frac{K_{hnf}}{K_f}(1 + \frac{4}{3}Rd)\theta'(0), \theta(\infty) = 0. \tag{12}$$

Some physical quantities of interest are melting rate at stretching sheet or Nusselt number Nu_x and skin friction C_f. The skin friction drag is presented as $C_f = \frac{\tau_w}{\rho_f U_w^2}$, the ratio of conductive and convective heat transfer rate is defined as $Nu_x = \frac{xq_w}{k(T_\infty - T_w)}$. The surface shear stress and heat flux are presented as below:

$$\tau_w = \mu_f\left(\frac{1}{(1-\phi_1)^{2.5}(1-\phi_2)^{2.5}} + \frac{1}{\beta_1}\right)\left(\frac{\partial u}{\partial y}\right)_{y=0}, q_w = -k_{hnf}\left(1 + \frac{4}{3}\right)\left(\frac{\partial T}{\partial y}\right)_{y=0}.$$

Using Eq (8), the above quantities become as

$$Re_x^{1/2}C_f = \left(\frac{1}{(1-\phi_1)^{2.5}(1-\phi_2)^{2.5}} + \frac{1}{\beta_1}\right)F''(0), Re_x^{1/2}Nu_x = -k_{hnf}\left(1 + \frac{4}{3}\right)\theta'(0).$$

The local Reynolds number is $Re_x = \frac{U_w x}{\nu}$. Some expressions are presented as:

$$\frac{\mu_{hnf}}{\mu_f} = \frac{1}{(1-\phi_1)^{2.5}(1-\phi_2)^{2.5}}, \ \frac{\rho_{hnf}}{\rho_f} = (1-\phi_1)(1-\phi_2) + \phi_1\frac{\rho_{s_1}}{\rho_f} + \phi_2\frac{\rho_{s_2}}{\rho_f},$$

$$\frac{(\rho C_p)_{hnf}}{(\rho C_p)_f} = (1-\phi_1)(1-\phi_2) + \phi_1\frac{(\rho C_p)_{s_1}}{(\rho C_p)_f} + \phi_2\frac{(\rho C_p)_{s_2}}{(\rho C_p)_f}.$$

The thermophysical characteristics of base fluid and nanoparticles in Table 1(see [21]).

Table 1. Thermophysical characteristics of base fluid and nanoparticles.

Physical properties	Base fluid	Nanoparticles	
	Water	SWCNTs	MWCNTs
$C_p\left(J/kg\ K\right)$	4179.0	425.00	796.0
$\rho(kg/m^3)$	997.10	2600.0	1600.0
$K(W/mK)$	0.6130	6600.0	3000.0

2.1. Numerical procedure

The system of differential equations is a nonlinear boundary value problem. Several methods have been applied to solve the nonlinear boundary value problem arising in fluid dynamics. The system of nonlinear higher-order differential equations subject to boundary conditions is solved through the fifth-order Runge-Kutta-Fehlberg approach. The higher-order nonlinear differential equations are transformed into first-order differential equations. The procedure of the transformed equations is as follows (see [30]):

$$y(1) = f(\eta), y(2) = f'(\eta), y(3) = f''(\eta), yy_1 = f'''(\eta), \tag{13}$$

$$yy_1 = [\mathrm{M}\{y(2) - 1\} - \frac{\rho_f \gamma}{\rho_{hnf}}\{2(y^2(5) - 1) - y(4).y(6)\} - 2(1 - y(2) - y(3).y(1) +$$

$$\delta y(7)]\frac{\rho_{hnf}}{\rho_f}.\left[\frac{1}{(1-\phi_1)^{2.5}(1-\phi_2)^{2.5}} + \frac{1}{\beta_1})^{-1}\right], \tag{14}$$

$$y(4) = g(\eta), y(5) = g'(\eta), y(6) = g''(\eta), yy_2 = g'''(\eta), \tag{15}$$

$$yy_2 = [y(6).y(1) - y(4).y(3)]\frac{1}{\lambda}, \tag{16}$$

$$y(7) = \theta(\eta), y(8) = \theta'(\eta), yy_3 = \theta''(\eta), \tag{17}$$

$$yy_3 = -[y(1).y(8) - \frac{(\rho_{cp})_f}{(\rho_{cp})_{hnf}}Ky(7)]\frac{K_f}{K_{hnf}}\frac{(\rho_{cp})_{hnf}}{(\rho_{cp})_f}Pr[1 + \frac{4}{3}Rd]^{-1}. \tag{18}$$

With boundary conditions are

$$y0(1) - S; y0(2) - \lambda_1\left(\frac{1}{(1-\phi_1)^{2.5}(1-\phi_2)^{2.5}} + \frac{1}{\beta_1}\right)y0(3); \ yinf(2) - 1; \ y0(4); y0(5); yinf(5) -$$

$$1; \ y0(7) - 1 - \delta_1\frac{K_{hnf}}{K_f}(1 + \frac{4}{3}Rd)y0(8); yinf(7). \tag{19}$$

The fifth-order Runge-Kutta-Fehlberg approach is used to solve the nonlinear higher-order differential system. The numerical outcomes will converge if the boundary residuals $(R_1(u^*{}_1, u^*{}_2, u^*{}_3), \ R_2(u^*{}_1, u^*{}_2, u^*{}_3), \ R_3(u^*{}_1, u^*{}_2, u^*{}_3))$ are not more than tolerance error i.e., 10^{-6}. Newton's approach is used to change the initial approximations, and it is repeated until the required convergence basis is met. The residuals of boundary are offered as below:

$$R_1(u^*{}_1, u^*{}_2, u^*{}_3) = |y_2(\infty) - \widehat{y_2}(\infty)|,$$

$$R_2(u^*{}_1, u^*{}_2, u^*{}_3) = |y_5(\infty) - \widehat{y_5}(\infty)|,$$

$$R_3(u^*{}_1, u^*{}_2, u^*{}_3) = |y_7(\infty) - \widehat{y_7}(\infty)|.$$

Hence, $\widehat{y_2}(\infty)$, $\widehat{y_5}(\infty)$, and $\widehat{y_7}(\infty)$ are computed boundary values. Validation of the numerical scheme using the grid-independent test. The models of hybrid nanofluid are introduced. The Yamada-Ota model expression is defined as below (see [14]):

$$\frac{k_{bf}}{k_f} = \frac{1 + \frac{k_f}{k_{s_1}} \frac{L}{R} \phi_1^{0.2} + \left(1 - \frac{k_f}{k_{s_1}}\right) \phi_1 \frac{L}{R} \phi_1^{0.2} + 2\phi_1 \left(\frac{k_{s_1}}{k_{s_1} - k_f}\right) ln\left(\frac{k_{s_1} + k_f}{2k_{s_1}}\right)}{1 - \phi_1 + 2\phi_1 \left(\frac{k_f}{k_{s_1} - k_f}\right) ln\left(\frac{k_{s_1} + k_f}{2k_f}\right)},$$

$$\frac{k_{hnf}}{k_{bf}} = \frac{1 + \frac{k_{bf}}{k_{s_2}} \frac{L}{R} \phi_2^{0.2} + \left(1 - \frac{k_{bf}}{k_{s_2}}\right) \phi_2 \frac{L}{R} \phi_2^{0.2} + 2\phi_2 \left(\frac{k_{s_2}}{k_{s_2} - k_{bf}}\right) ln\left(\frac{k_{s_2} + k_{bf}}{2k_{s_2}}\right)}{1 - \phi_2 + 2\phi_2 \left(\frac{k_{bf}}{k_{s_2} - k_{bf}}\right) ln\left(\frac{k_{s_2} + k_{bf}}{2k_{bf}}\right)}.$$

Xue model expression is defined as below:

$$\frac{k_{bf}}{k_f} = \frac{1 - \phi_1 + 2\phi_1 \left(\frac{k_{s_1}}{k_{s_1} - k_f}\right) ln\left(\frac{k_{s_1} + k_f}{2k_f}\right)}{1 - \phi_1 + 2\phi_1 \left(\frac{k_f}{k_{s_1} - k_f}\right) ln\left(\frac{k_{s_1} + k_f}{2k_f}\right)},$$

$$\frac{k_{hnf}}{k_{bf}} = \frac{1 - \phi_2 + 2\phi_2 \left(\frac{k_{s_2}}{k_{s_2} - k_{bf}}\right) ln\left(\frac{k_{s_2} + k_{bf}}{2k_{bf}}\right)}{1 - \phi_2 + 2\phi_2 \left(\frac{k_{bf}}{k_{s_2} - k_{bf}}\right) ln\left(\frac{k_{s_2} + k_{bf}}{2k_{bf}}\right)}.$$

Tiwari-Das model expression is defined as below:

$$\frac{k_{bf}}{k_f} = \frac{(n-1)k_f - (k_f - k_{s_1})\phi_1(n-1) + k_{s_1}}{(k_f - k_{s_1})\phi_1 + (n-1)k_f + k_{s_1}},$$

$$\frac{k_{hnf}}{k_{bf}} = \frac{(n-1)k_{bf} - (k_{bf} - k_{s_2})\phi_2(n-1) + k_{s_2}}{(k_{bf} - k_{s_2})\phi_2 + (n-1)k_{bf} + k_{s_2}}.$$

3. Results and discussion

A system of nonlinear ordinary differential Eqs (9)–(11) with boundary conditions (12) is solved through a numerical technique using the Matlab software packages. The involving physical parameters namely: M porosity parameter, β_1 Casson fluid parameter, γ_1 magnetic parameter, δ bouncy force parameter, λ reciprocal magnetic Prandtl number, Pr Prandtl number, K heat generation, Rd radiation parameter, S suction parameter, λ_1 velocity slip parameter, and δ_1 thermal slip parameter effects on the velocity profile, induced magnetic profile and temperature profile are revealed through Figures 2–13. In this analysis, we considered three models of hybrid nanofluid, namely: the Xue, Tiwari Das, and Yamada-Ota models. Two kinds of nanoparticles are discussed: single-wall and multi-wall carbon nanotubes with base fluid water. Thermo-physical characteristics of base fluid and nanoparticles are used which are revealed in Table 1. The variation of the velocity profile and β_1 is shown in Figure 2. The curves of the velocity profile declined due to increasing the values of the Casson fluid parameter. The viscosity of fluid increased due to an increment in the Casson fluid parameter, which ultimately reduced the velocity of the fluid at the permeable vertical Riga sheet. The influence of γ_1 on the velocity function is presented in Figure 3. The velocity profile curves decrease as the values of γ_1 rise. As the electromagnetic forces enhanced due to increment of magnetic parameter which declined the velocity function.
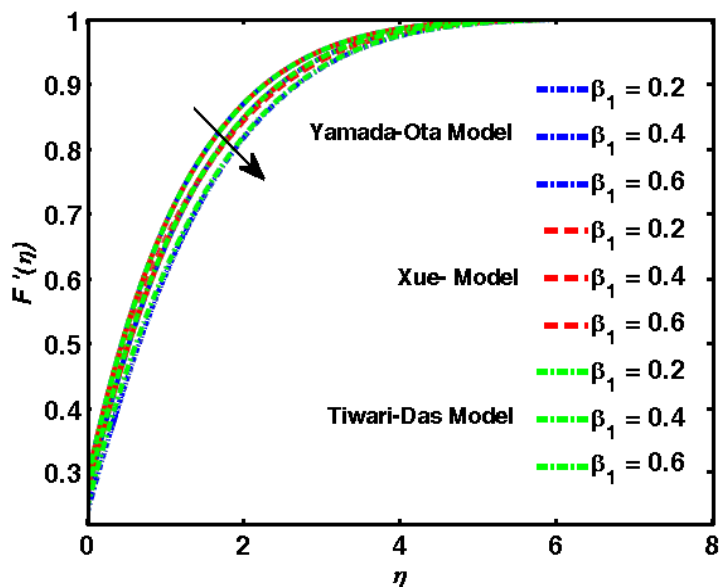
Figure 2. Effect of β_1 on the $F'(\eta)$.
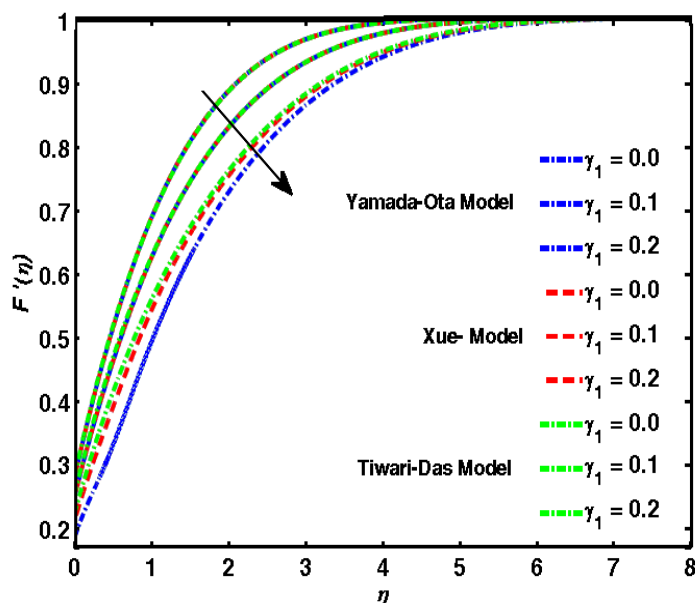
Figure 3. Effect of γ_1 on the $F'(\eta)$.

The impacts of λ_1 on the velocity profile are revealed in Figure 4. The velocity profile increased due to growing values of λ_1. This is due to the fact that when the slip condition arises, the velocity of the stretching sheet is different from the flow velocity nearby. The variation of the porosity parameter and the velocity profile is presented in Figure 5. It is prominent that the velocity function declined due to enhancing values of the porosity parameter. The velocity boundary layer thickness increases with the porosity value, reducing the fluid flow resistance.
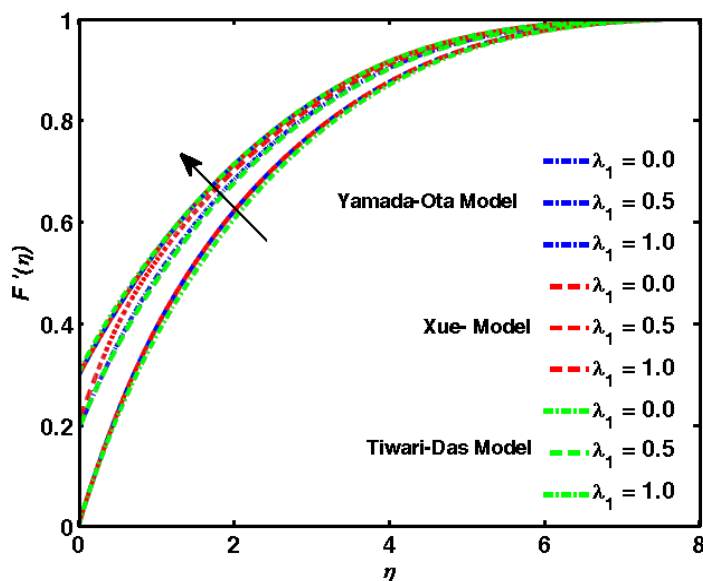
Figure 4. Effect of λ_1 on the $F'(\eta)$.
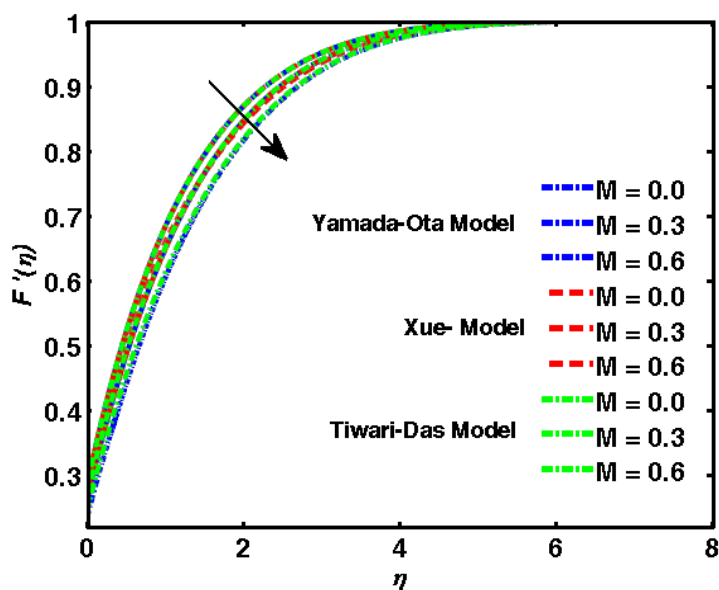
Figure 5. Effect of M on the $F'(\eta)$.

Figure 6 highlights the influence of ϕ_2 on the velocity profile. The curves of the velocity profile decline due to higher values of ϕ_2. As a result, the magneto-Casson hybrid nanofluid's effective viscosity increases for positive values of the nanoparticle volume fraction and exhibits high resistance to liquid motion. The impact of solid nanoparticles concentration on the induced magnetic profile is presented in Figure 7. The induced magnetic profile declined due to increasing values of solid nanoparticle concentration. The magnetic field provides an impulse to the fluid that is being slowed down by viscous force as well as stabilizing the viscous impacts.
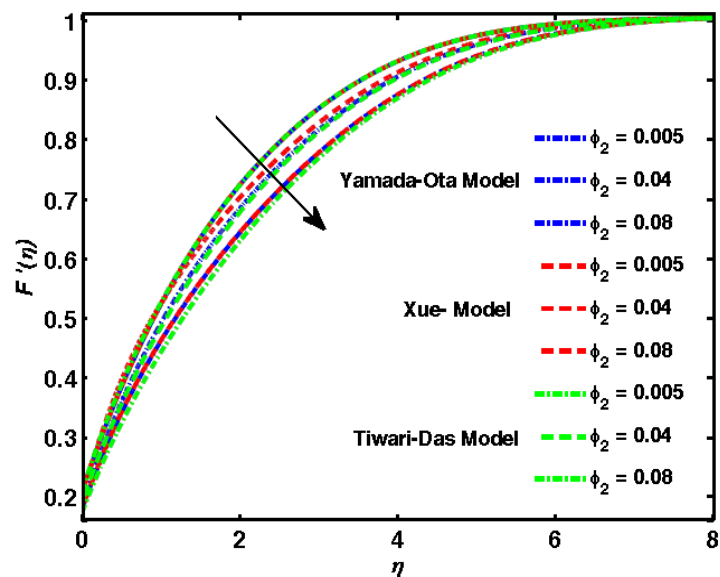
Figure 6. Effect of ϕ_2 on the $F'(\eta)$.
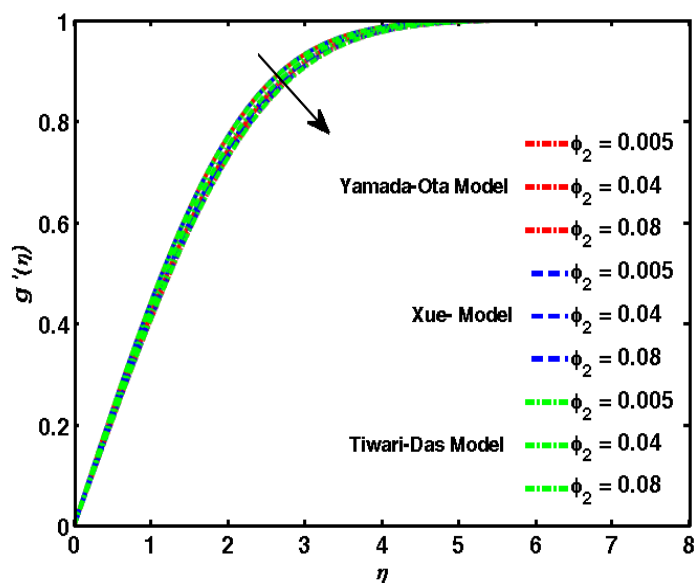
Figure 7. Effect of ϕ_2 on the $g'(\eta)$.

The variation of the magnetic Prandtl number with the induced magnetic profile is revealed in Figure 8. The induced magnetic profile increased due to increasing values of magnetic Prandtl number. The variation of the bouncy force parameter with temperature function is shown in Figure 9. The temperature profile increased due to rising values of the bouncy force parameter.
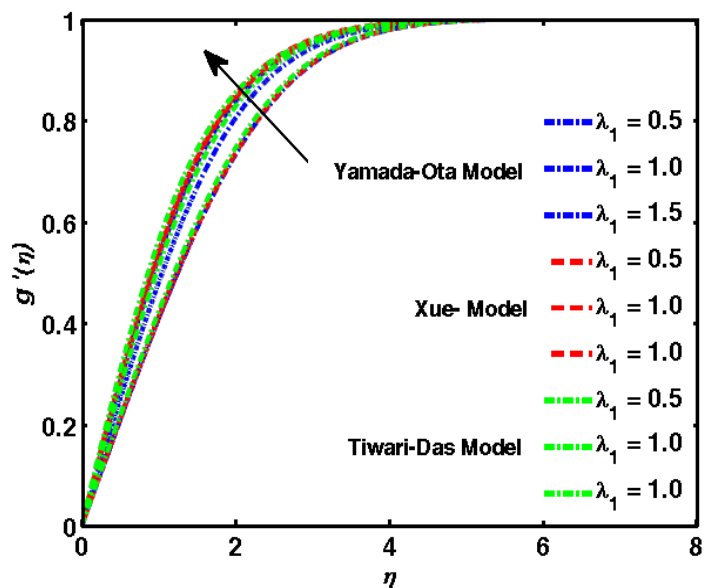
Figure 8. Effect of λ_1 on the $g'(\eta)$.
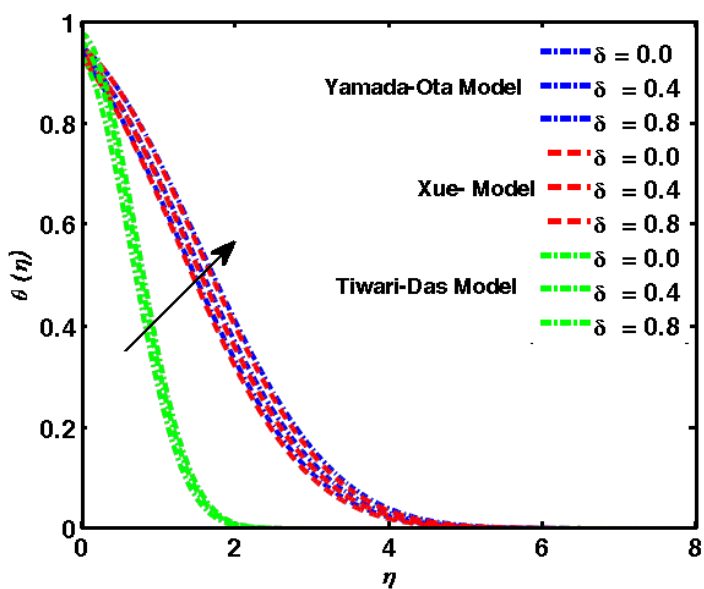
Figure 9. Effect of δ on the $\theta(\eta)$.

Figure 10 exposes the influence of thermal slip on the temperature profile. The curves of the temperature profile decline due to increasing values of thermal slip. The influence of K on the temperature profile is illustrated in Figure 11. As heat generation increased, the temperature function at permeable vertical sheet improved.
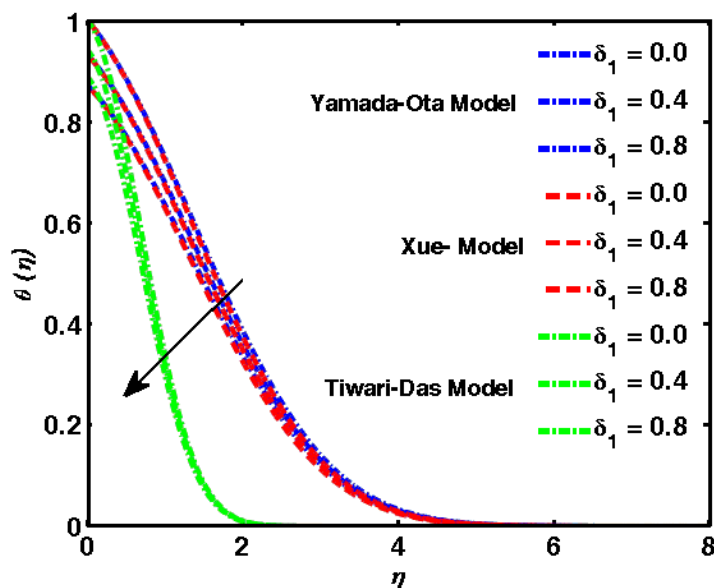
Figure 10. Effect of δ_1 on the $\theta(\eta)$.
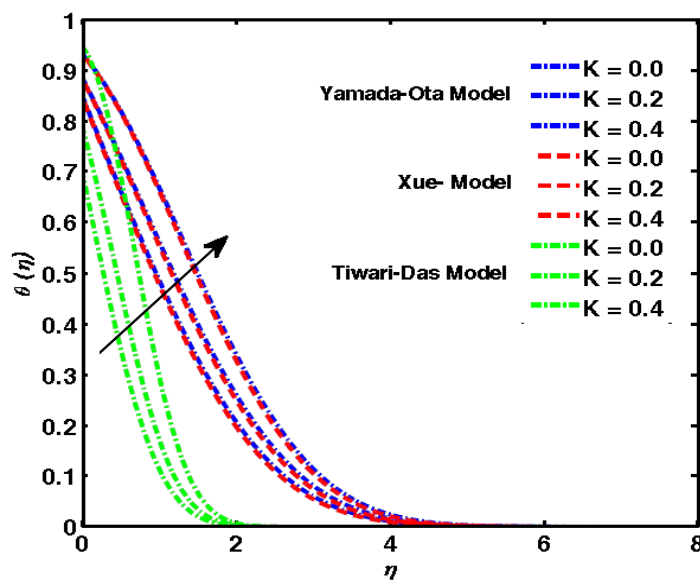
Figure 11. Effect of K on the $\theta(\eta)$.

Figure 12 shows the impacts of Rd on the temperature profile. The curves of the temperature profile increased due to larger values of the radiation parameter. Radiation is a heat exchanger between two surfaces. As the temperature enhanced due to enhancing the values of radiation parameters. The variation of ϕ_2 with the temperature profile is presented in Figure 13. The temperature profile shows an inciting nature towards higher concentration of solid nanoparticles. Because the thermal conductivity of the fluid was enhanced due to an increment in solid nanoparticles, which enhanced the temperature of the magneto-Casson hybrid nanofluid.
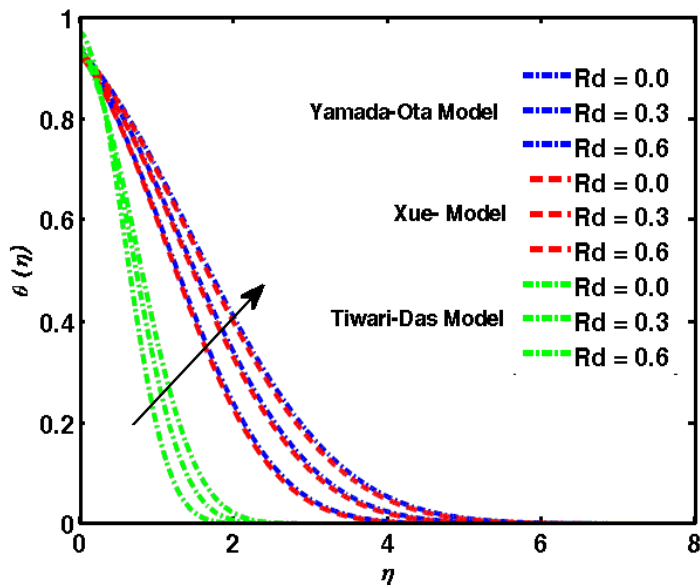
Figure 12. Effect of Rd on the $\theta(\eta)$.
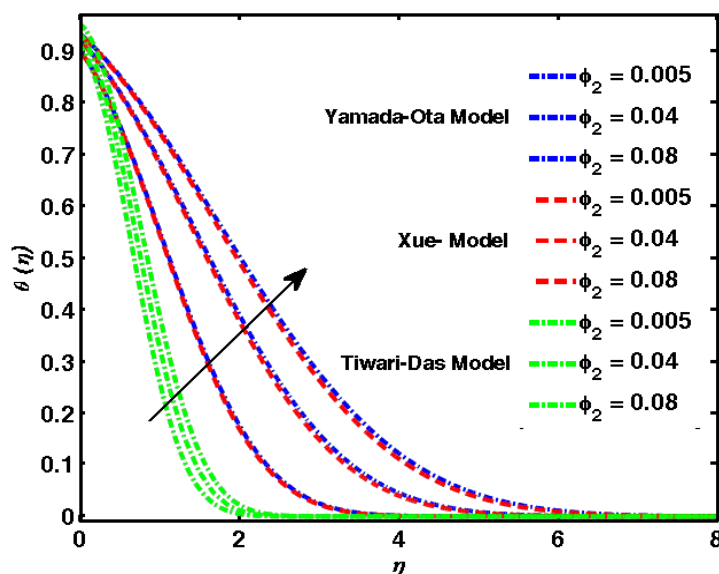
Figure 13. Effect of ϕ_2 on the $\theta(\eta)$.

The involving physical parameters, namely: M porosity parameter, β_1 Casson fluid parameter, γ_1 magnetic parameter, δ bouncy force parameter, λ_1 reciprocal magnetic Prandtl number, Pr Prandtl number, K heat generation, Rd radiation parameter, S suction parameter, λ velocity slip parameter, and δ_1 thermal slip parameter effects on the skin friction and Nusselt number are presented in Tables 2 and 3. The variation of the thermal slip with skin friction is presented in Table 2. The values of thermal slip are enhanced which increases skin friction. The inspiration of Rd for skin friction is revealed in Table 2. The values of skin friction increased due to higher values of radiation parameters. As the radiation is enhanced it resists to enhance the skin friction.

Table 2. Comparative numerical analysis of the Yamada-Ota model, Tiwari-Das model, and Xue model for skin friction with physical parameters.

δ_1	Rd	K	γ_1	M	δ	λ_1	β_1	λ	ϕ_2	S	Yamada-Ota Model	Xue-Model	Tiwari-Das Model
0.2	04	0.4	0.1	0.3	0.5	0.4	0.3	0.5	0.04	0.4	3.9277	3.9265	3.8982
0.4	-	-	-	-	-	-	-	-	-	-	3.9331	3.9321	3.9217
0.6	-	-	-	-	-	-	-	-	-	-	3.9379	3.9371	3.9378
0.4	0.2	-	-	-	-	-	-	-	-	-	3.9293	3.9284	3.9259
-	0.4	-	-	-	-	-	-	-	-	-	3.9331	3.9321	3.9217
-	0.6	-	-	-	-	-	-	-	-	-	3.9364	3.9354	3.9191
-	0.4	0.0	-	-	-	-	-	-	-	-	3.9284	3.9278	3.9321
-	-	0.2	-	-	-	-	-	-	-	-	3.9302	3.9294	3.9276
-	-	0.4	-	-	-	-	-	-	-	-	3.9331	3.9321	3.9217
-2	-	0.6	-	-	-	-	-	-	-	-	3.9380	3.9368	3.9130
-	-	0.4	0.1	-	-	-	-	-	-	-	3.9331	3.9321	3.9217
-	-	-	0.3	-	-	-	-	-	-	-	3.1784	3.1774	3.1647
-	-	-	0.5	-	-	-	-	-	-	-	2.3019	2.3008	2.2825
-	-	-	0.1	0.0	-	-	-	-	-	-	4.2479	4.2479	4.2479
-	-	-	-	0.3	-	-	-	-	-	-	3.9331	3.9321	3.9217
-	-	-	-	0.6	-	-	-	-	-	-	3.5766	3.5746	3.5555
-	-	-	-	0.3	0.0	-	-	-	-	-	4.0232	4.0232	3.9422
-	-	-	-	-	0.5	-	-	-	-	-	3.9331	3.9321	3.8047
-	-	-	-	-	1.0	-	-	-	-	-	3.8436	3.8416	3.6662
-	-	-	-	-	0.5	0.2	-	-	-	-	3.8979	3.8969	3.7675
-	-	-	-	-	-	0.4	-	-	-	-	3.9331	3.9321	3.8047
-	-	-	-	-	-	0.6	-	-	-	-	3.9540	3.9530	3.8266
-	-	-	-	-	-	0.4	0.1	-	-	-	5.8775	5.8766	5.6973
-	-	-	-	-	-	-	0.3	-	-	-	3.9331	3.9321	3.8047
-	-	-	-	-	-	-	0.5	-	-	-	3.5737	3.5727	3.4533
-	-	-	-	-	-	-	0.3	0.0	-	-	5.2763	5.2749	5.0492
-	-	-	-	-	-	-	-	0.5	-	-	3.9331	3.9321	3.8047
-	-	-	-	-	-	-	-	1.0	-	-	3.1172	3.1165	3.0330
-	-	-	-	-	-	-	-	0.5	0.005	-	3.3073	3.3070	3.2240
-	-	-	-	-	-	-	-	-	0.02	-	3.5631	3.5625	3.4621
-	-	-	-	-	-	-	-	-	0.04	-	3.9331	3.9321	3.8047
-	-	-	-	-	-	-	-	-	0.06	-	4.3394	4.3381	4.1788
-	-	-	-	-	-	-	-	-	0.04	0.0	3.6943	3.6933	3.5161
-	-	-	-	-	-	-	-	-	-	0.2	3.8118	3.8108	3.6568
-	-	-	-	-	-	-	-	-	-	0.4	3.9331	3.9321	3.8047
-	-	-	-	-	-	-	-	-	-	0.6	4.0575	4.0567	3.9526

Table 3. Comparative numerical analysis of Yamada-Ota model, Tiwari-Das model, and Xue model for Nusselt number with physical parameters.

| Physical parameters | | | | | | | | | | | $Re_x^{1/2}Nu_x$ | | |
δ_1	Rd	K	γ_1	M	δ	λ_1	β_1	λ	ϕ_2	S	Yamada-Ota Model	Xue-Model	Tiwari-Das Model
0.2	04	0.4	0.1	0.3	0.5	0.4	0.3	0.5	0.04	0.4	3.5558	3.4796	1.8070
0.4	-	-	-	-	-	-	-	-	-	-	3.3573	3.2804	1.4694
0.6	-	-	-	-	-	-	-	-	-	-	3.1795	3.1024	1.2376
0.4	0.2	-	-	-	-	-	-	-	-	-	3.0678	3.0002	1.3549
-	0.4	-	-	-	-	-	-	-	-	-	3.3573	3.2804	1.4694
-	0.6	-	-	-	-	-	-	-	-	-	3.6307	3.5450	1.5672
-	0.4	0.0	-	-	-	-	-	-	-	-	5.4398	5.3008	1.8099
-	-	0.2	-	-	-	-	-	-	-	-	4.5319	4.4212	1.6671
-	-	0.4	-	-	-	-	-	-	-	-	3.3573	3.2804	1.4694
-	-	0.6	-	-	-	-	-	-	-	-	1.7182	1.6821	1.1640
-	-	0.4	0.1	-	-	-	-	-	-	-	3.3573	3.2804	1.4694
-	-	-	0.3	-	-	-	-	-	-	-	2.8416	2.7778	1.3849
-	-	-	0.5	-	-	-	-	-	-	-	1.9747	1.9312	1.2451
-	-	-	0.1	0.0	-	-	-	-	-	-	3.5143	3.4338	1.4973
-	-	-	-	0.3	-	-	-	-	-	-	3.3573	3.2804	1.4694
-	-	-	-	0.6	-	-	-	-	-	-	3.1609	3.0883	1.4347
-	-	-	-	0.3	0.0	-	-	-	-	-	3.4099	3.3318	1.4704
-	-	-	-	-	0.5	-	-	-	-	-	3.3573	3.2804	1.4587
-	-	-	-	-	1.0	-	-	-	-	-	3.3036	3.2278	1.4465
-	-	-	-	-	0.5	0.2	-	-	-	-	3.3233	3.2475	1.4544
-	-	-	-	-	-	0.4	-	-	-	-	3.3573	3.2804	1.4587
-	-	-	-	-	-	0.6	-	-	-	-	3.3762	3.2986	1.4612
-	-	-	-	-	-	0.4	0.0	-	-	-	2.5806	2.5223	1.3223
-	-	-	-	-	-	-	0.3	-	-	-	3.3573	3.2804	1.4587
-	-	-	-	-	-	-	0.6	-	-	-	3.6019	3.5190	1.5034
-	-	-	-	-	-	-	0.3	0.0	-	-	2.5647	2.4973	1.1972
-	-	-	-	-	-	-	-	0.5	-	S	3.3573	3.2804	1.4587
-	-	-	-	-	-	-	-	1.0	-	-	3.7602	3.6767	1.5657
-	-	-	-	-	-	-	-	0.5	.005	-	2.5001	2.4666	1.4006
-	-	-	-	-	-	-	-	-	0.02	-	2.8923	2.8389	1.4266
-	-	-	-	-	-	-	-	-	0.04	-	3.3573	3.2804	1.4587
-	-	-	-	-	-	-	-	-	0.06	-	3.7799	3.6816	1.4876
-	-	-	-	-	-	-	-	-	0.04	0.0	1.6248	1.5507	0.196851
-	-	-	-	-	-	-	-	-	-	0.2	2.5003	2.4258	0.85367
-	-	-	-	-	-	-	-	-	-	0.4	3.3573	3.2804	1.4587
-	-	-	-	-	-	-	-	-	-	0.6	4.1876	4.1061	1.8678

The influence of K on skin friction is highlighted in Table 2. The values of skin friction increased

due to higher values of the heat generation parameter. Table 2 reveals the variation of porosity parameters and skin friction. The values of skin friction decline due to higher values of the porosity parameter. The porous body's pore volume to total nominal volume ratio resists decreasing skin friction. The impact of the bouncy force parameter on the skin friction reveals in Table 2. The values of skin friction are reduced due to higher values of the bouncy force parameter. A body submerged partially or completely in a fluid appears to drop weight or to be lighter due to the buoyant force.

The impact of velocity slip on skin friction is revealed in Table 2. Values of skin friction increased due to higher values of λ_1. This is due to the fact that when the slip condition arises, the velocity of the stretching sheet is different from the flow velocity nearby as well as skin friction is enhanced. Table 2 reveals the influence of the Casson fluid parameter on skin friction. The skin friction declines due to larger values of β_1. The variation of the magnetic Prandtl number and skin friction is presented in Table 2. The skin friction is found to be decreasing behavior due to higher values of magnetic Prandtl number. The influence of ϕ_2 on skin friction is revealed in Table 2. The values of skin friction are found to be increasing due to higher values of ϕ_2 because of solid particles in the fluid are enhanced, which increases the skin friction phenomena.

The variation of suction parameters with skin friction is revealed in Table 2. The values of skin friction increased due to larger values of S because the section parameter enhanced, which resisted the flow of fluid as well as enhanced skin friction. The influence of thermal slip on the Nusselt number is revealed in Table 3. The values of the Nusselt number increased due to enhancing values of δ_1. The variation of radiation parameter and Nusselt number is revealed in Table 3. The values of the Nusselt number are enhanced due to boosting values of the radiation parameter. As a result of the addition of radiation, the heat transfer phenomenon was enhanced. The impacts of heat generation on the Nusselt number are presented in Table 3. The heat generation parameter is enhanced, which declines the values of the Nusselt number. The impacts of magnetic parameters on the Nusselt number are revealed in Table 3. The values of the Nusselt number are found to be declining due to higher values of the magnetic field parameter.

The variation of the porosity parameter and Nusselt number is revealed in Table 3. The values of the Nusselt number are reduced due to porosity parameter enhancement. The variation of δ bouncy force parameter and Nusselt number are presented in Table 3. The values of the Nusselt number decay due to greater values of δ bouncy force parameter. The influence of velocity slip on the Nusselt number is shown in Table 3. The values of the Nusselt number are enhanced due to higher values of λ_1. The variation of β_1 and Nusselt number reveals in Table 3. As the value of the β_1 grew, the Nusselt number moved up. The impact of the magnetic Prandtl number on the Nusselt number is revealed in Table 3. The Nusselt number enhances for higher values of λ.

The influence of solid nanoparticle concentration on the Nusselt number is shown in Table 3. The heat transfer rate enhances due to higher values of ϕ_2. The thermal conductivity of the fluid increased due to the increment in solid nanoparticles in the base fluid, which boosted the values of the heat transfer rate. The inspiration of the suction parameter on the Nusselt number is highlighted in Table 3. The Nusselt number rises as the value of the suction parameter rises. Table 4 offers the comparative results of Zainal et al. [33] and Bachok et al. [34] for various values ϕ_2 on skin friction when the rest of values are zero such as $M = \gamma_1 = \delta = \lambda_1 = K = Rd = S = \lambda = \delta_1 = \phi_1 = 0$ and $\beta_1 \to \infty$. It should be noted that our results were found to be in good agreement with existing results.

Table 4. Comparison with Zainal et al. [33] and Bachok et al. [34] for different values ϕ_2 on the skin friction when the rest of values are zero such as $M = \gamma_1 = \delta = \lambda_1 = K = Rd = S = \lambda = \delta_1 = \phi_1 = 0$ and $\beta_1 \to \infty$.

ϕ_2	Zainal et al. [33]	Bachok et al. [34]	Present results
0.0	1.687218	1.687200	1.687221
0.1	2.579342	2.579400	2.579317
0.2	3.590122	3.590100	3.590111

4. Conclusions

In this analysis, the steady flow of hybrid Casson nanofluid over a vertical permeable exponential stretching sheet is considered. The impacts of the induced magnetic field are studied in this analysis. The influence of heat generation and radiation with a slip effect is studied. Three models of hybrid nanofluid, namely: Yamada-Ota, Xue, and Tiwari Das are debated. The key points are presented as follows:

- The skin friction achieved higher values in the Yamada-Ota model of hybrid nanofluid as compared to the Xue model and the Tiwari Das model.
- The Nusselt number achieved higher values in the Yamada-Ota model of hybrid nanofluid as compared to the Xue model and Tiwari Das model.
- Temperature profile increased due to larger values of the radiation parameter. Radiation is a heat exchanger between two surfaces.
- The temperature profile shows in inciting nature towards higher concentration of nanoparticles. Because the thermal conductivity of the fluid was enhanced due to an increment in solid nanoparticles, which enhanced the temperature of magneto-Casson hybrid nanofluid.
- The velocity profile increased due to increasing the values of λ_1. This is due to the fact that when the slip condition arises, the velocity of the stretching sheet is different from the flow velocity nearby.
- The velocity profile declined due to increasing the values of the Casson fluid parameter. Higher values of the Casson fluid parameter cause a reduction in viscosity of the fluid as a result velocity reduces.
- The values of skin friction are found to be increasing due to higher values of ϕ_2 because solid particles in the fluid are enhanced, which increases the skin friction coefficient.

Acknowledgments

Conflict of interest

The authors declare no conflict of interest.

References

[1] M. Hamad, M. Bashir, Boundary-layer flow and heat transfer of a power-law non-Newtonian nanofluid over a vertical stretching sheet, *World Applied Sciences Journal*, **7** (2009), 172–178.

[2] N. Bachok, A. Ishak, I. Pop, Boundary-layer flow of nanofluids over a moving surface in a flowing fluid, *Int. J. Therm. Sci.*, **49** (2010), 1663–1668. https://doi.org/10.1016/j.ijthermalsci.2010.01.026

[3] S. Nadeem, C. Lee, Boundary layer flow of nanofluid over an exponentially stretching surface, *Nanoscale Res. Lett.*, **7** (2012), 94. https://doi.org/10.1186/1556-276X-7-94

[4] O. Anwar Bég, M. Khan, I. Karim, Md. Alam, M. Ferdows, Explicit numerical study of unsteady hydromagnetic mixed convective nanofluid flow from an exponentially stretching sheet in porous media, *Appl. Nanosci.*, **4** (2014), 943–957. https://doi.org/10.1007/s13204-013-0275-0

[5] G. Ramesh, Darcy-Forchheimer flow of Casson nanofluid with heat source/sink: a three-dimensional study, In *Heat and mass transfer-advances in modelling and experimental study for industrial applications*, London: Intech Open, 2018, 43–62. https://doi.org/10.5772/intechopen.74170

[6] M. Khan, S. Nadeem, A comparative study between linear and exponential stretching sheet with double stratification of a rotating Maxwell nanofluid flow, *Surf. Interfaces*, **22** (2021), 100886. https://doi.org/10.1016/j.surfin.2020.100886

[7] M. Khan, R. Ali, H. Ahmad, N. Abbas, A. Mousa, A. Galal, Thermal and chemically reactive features of Casson nanofluid flow with thermophoresis and Brownian effect over an exponentially stretching surface, *P. I. Mech. Eng. E-J. Pro.*, in press. https://doi.org/10.1177/09544089211064465

[8] G. Ramesh, G. Roopa, A. Rauf, S. Shehzad, F. Abbasi, Time-dependent squeezing flow of Casson-micropolar nanofluid with injection/suction and slip effects, *Int. Commun. Heat Mass*, **126** (2020), 105470. https://doi.org/10.1016/j.icheatmasstransfer.2021.105470

[9] F. Wang, S. Ahmad, Q. Al Mdallal, M. Alammari, M. Khan, A. Rehman, Natural bio-convective flow of Maxwell nanofluid over an exponentially stretching surface with slip effect and convective boundary condition, *Sci. Rep.*, **12** (2022), 2220. https://doi.org/10.1038/s41598-022-04948-y

[10] L. Ali, B. Ali, X. Liu, T. Iqbal, R. Zulqarnain, M. Javid, A comparative study of unsteady MHD Falkner-Skan wedge flow for non-Newtonian nanofluids considering thermal radiation and activation energy, *Chinese J. Phys.*, **77** (2022), 1625–1638. https://doi.org/10.1016/j.cjph.2021.10.045

[11] S. Anjali Devi, S. Suriya Uma Devi, Numerical investigation of hydromagnetic hybrid Cu-Al_2O_3/water nanofluid flow over a permeable stretching sheet with suction, *Int. J. Nonlin. Sci. Num.*, **17** (2016), 249–257. https://doi.org/10.1515/ijnsns-2016-0037

[12] S. Nadeem, N. Abbas, A. Khan, Characteristics of three dimensional stagnation point flow of Hybrid nanofluid past a circular cylinder, *Results Phys.*, **8** (2018), 829–835. https://doi.org/10.1016/j.rinp.2018.01.024

[13] S. Nadeem, N. Abbas, M. Malik, Inspection of hybrid based nanofluid flow over a curved surface, *Comput. Meth. Prog. Bio.*, **189** (2020), 105193. https://doi.org/10.1016/j.cmpb.2019.105193

[14] N. Abbas, S. Nadeem, A. Saleemc, M. Malik, A. Issakhov, F. Alharbi, Models base study of inclined MHD of hybrid nanofluid flow over nonlinear stretching cylinder, *Chinese J. Phys.*, **69** (2021), 109–117. https://doi.org/10.1016/j.cjph.2020.11.019

[15] A. Jyothi, R. Varun Kumar, J. Madhukesh, B. Prasannakumara, G. Ramesh, Squeezing flow of Casson hybrid nanofluid between parallel plates with a heat source or sink and thermophoretic particle deposition, *Heat Transf.*, **50** (2021), 7139–7156. https://doi.org/10.1002/htj.22221

[16] V. Puneeth, S. Manjunatha, J. Madhukesh, G. Ramesh, Three dimensional mixed convection flow of hybrid casson nanofluid past a non-linear stretching surface: a modified Buongiorno's model aspects, *Chaos Soliton. Fract.*, **152** (2021), 111428. https://doi.org/10.1016/j.chaos.2021.111428

[17] P. Li, F. Duraihem. A. Awan, A. Al-Zubaidi, N. Abbas, D. Ahmad, Heat transfer of hybrid nanomaterials base Maxwell micropolar fluid flow over an exponentially stretching surface, *Nanomaterials*, **12** (2022), 1207. https://doi.org/10.3390/nano12071207

[18] F. Ali, R. Nazar, N. Arifin, I. Pop, MHD boundary layer flow and heat transfer over a stretching sheet with induced magnetic field, *Heat Mass Transfer*, **47** (2011), 155–162. https://doi.org/10.1007/s00231-010-0693-4

[19] G. Thammanna, K. Kumar, B. Gireesha, G. Ramesh, B. Prasannakumara, Three dimensional MHD flow of couple stress Casson fluid past an unsteady stretching surface with chemical reaction, *Results Phys.*, **7** (2017), 4104–4110. https://doi.org/10.1016/j.rinp.2017.10.016

[20] M. Junoh, F. Ali, N. Arifin, N. Bachok, I. Pop, MHD stagnation-point flow and heat transfer past a stretching/shrinking sheet in a hybrid nanofluid with induced magnetic field, *Int. J. Numer. Method. H.*, **30** (2020), 1345–1364. https://doi.org/10.1108/HFF-06-2019-0500

[21] A. Al-Hanaya, F. Sajid, N. Abbas, S. Nadeem, Effect of SWCNT and MWCNT on the flow of micropolar hybrid nanofluid over a curved stretching surface with induced magnetic field, *Sci. Rep.*, **10** (2020), 5488. https://doi.org/10.1038/s41598-020-65278-5

[22] S. Alharbi, Impact of hybrid nanoparticles on transport mechanism in magnetohydrodynamic fluid flow exposed to induced magnetic field, *Ain Shams Eng. J.*, **12** (2021), 995–1000. https://doi.org/10.1016/j.asej.2020.04.013

[23] M. Hafeez, M. Krawczuk, K. Nisar, W. Jamshed, A. Pasha, A finite element analysis of thermal energy inclination based on ternary hybrid nanoparticles influenced by induced magnetic field, *Int. Commun. Heat Mass*, **135** (2022), 106074. https://doi.org/10.1016/j.icheatmasstransfer.2022.106074

[24] L. Ali, B. Ali, M. Ghori, Melting effect on Cattaneo-Christov and thermal radiation features for aligned MHD nanofluid flow comprising microorganisms to leading edge: FEM approach, *Comput. Math. Appl.*, **109** (2022), 260–269. https://doi.org/10.1016/j.camwa.2022.01.009

[25] L. Ali, B. Ali, X. Liu, S. Ahmed, M. Shah, Analysis of bio-convective MHD Blasius and Sakiadis flow with Cattaneo-Christov heat flux model and chemical reaction, *Chinese J. Phys.*, **77** (2022), 1963–1975. https://doi.org/10.1016/j.cjph.2021.12.008

[26] M. Anwar, H. Firdous, A. Al Zubaidi, N. Abbas, S. Nadeem, Computational analysis of induced magnetohydrodynamic non-Newtonian nanofluid flow over nonlinear stretching sheet, *Prog. React. Kinet. Mec.*, in press. https://doi.org/10.1177/14686783211072712

[27] A. Alghamdi, S. Gala, M. Ragusa, Regularity criterion for weak solutions to the Navier-Stokes involving one velocity and one vorticity components, *Sib. Electron. Math. Re.*, **19** (2022), 309–315.

[28] A. Alghamdi, S. Gala, M. Ragusa, Beale-Kato-Majda's criterion for magneto-hydrodynamic equations with zero viscosity, *Novi Sad J. Math*, **50** (2020), 89–97. https://doi.org/10.30755/NSJOM.09142

[29] G. Ramesh, B. Prasannakumara, B. Gireesha, M. Rashidi, Casson fluid flow near the stagnation point over a stretching sheet with variable thickness and radiation, *J. Appl. Fluid Mech.*, **9** (2016), 1115–1022. https://doi.org/10.18869/ACADPUB.JAFM.68.228.24584

[30] W. Khan, M. Awais, N. Parveen, A. Ali, S. Awan, M. Malik, et al., Analytical assessment of (Al_2O_3-Ag/H_2O) hybrid nanofluid influenced by induced magnetic field for second law analysis with mixed convection, viscous dissipation and heat generation, *Coatings*, **11** (2021), 498. https://doi.org/10.3390/coatings11050498

[31] N. Abbas, W. Shatanawi, K. Abodayeh, Computational analysis of MHD nonlinear radiation Casson hybrid nanofluid flow at vertical stretching sheet, *Symmetry*, **14** (2020), 1494. https://doi.org/10.3390/sym14071494

[32] L. Ali, X. Liu, B. Ali, S. Abdal, R. Zulqarnain, Finite element analysis of unsteady MHD Blasius and Sakiadis flow with radiation and thermal convection using Cattaneo-Christov heat flux model, *Phys. Scr.*, **96** (2021), 125219.

[33] N. Zainal, R. Nazar, K. Naganthran, I. Pop, Unsteady MHD stagnation point flow induced by exponentially permeable stretching/shrinking sheet of hybrid nanofluid, *Eng. Sci. Technol.*, **24** (2021), 1201–1210. https://doi.org/10.1016/j.jestch.2021.01.018

[34] N. Bachok, A. Ishak, I. Pop, The boundary layers of an unsteady stagnation-point flow in a nanofluid, *Int. J. Heat Mass*, **55** (2012), 6499–6505. https://doi.org/10.1016/j.ijheatmasstransfer.2012.06.050